Bollettino di Geofisica Teorica ed Applicata Vol. 61, n. 2, pp. 199-218; June 2020
DOI 10.4430/bgta0305

Determination of possible failure surfaces in an open-pit slope caused by underground production

M.V. Ozdogan and A.H. Deliormanli

Department of Mining Engineering, Dokuz Eylul University, Turkey

(Received: 10 January 2019; accepted: 21 October 2019)

ABSTRACT Assessment of open-pit slopes is important for identifying failure mechanisms and taking precautions before a serious slope failure. Especially in simultaneous underground and open-pit mining activities, unstable slopes are expected under the subsidence effect of underground production, independently of the current kinematical conditions of the pit slope. In these circumstances, the stability assessments must consider the effect of underground operation. The present study monitors the stability in an open-pit slope located above an underground mine by a terrestrial laser scanner (TLS), and compares the results with those of kinematical analyses. Although no failure was predicted in the kinematical analyses, significant deformation rates were detected by TLS. Depending on the subsidence effect of underground production, the minimum angle of open-pit slopes that cause the instability was determined, and the locations of possible failure were determined by a model created from the TLS measurements. The updated analyses revealed the possibility of plane, wedge, and block-toppling failures.

Key words: LiDAR, rock slope, monitoring, kinematic analysis, transect analyse.

1. Introduction

The slope stability of open-pit mines depends mainly on the geotechnical properties of the rock masses, orientation of the slopes, and the overall slope angle. By understanding the main reason of failure, we can undertake preventative safety studies.

Progressive deformation and brittle fracture damage are the precursory activities of rock slope failures (Stead *et al*., 2006). These processes are detected as surface and subsurface displacements (Angeli *et al*., 2000) and preliminary rockfalls along fractures defining the possible failure scar (Rosser *et al*., 2007). The acceleration of these processes prior to failure (Nishii and Matsuoka, 2010) provides a basis for failure time prediction (Fukuzono, 1990; Crosta and Agliardi, 2002; Petley *et al*., 2002; Petley, 2004). Deformation monitoring has also improved the understanding of deep-seated landslides (Agliardi *et al*., 2001), and the forecasting ability of slope failure in open-pit mines (Rose and Hungr, 2007). Furthermore, deformation monitoring is helpful for understanding the mechanisms and stability states of landslide failure, designing appropriate mitigation measures, and elucidating sensitivity to environmental triggers (Crosta and Agliardi, 2002; Eberhardt *et al*., 2010; Kromer *et al*., 2015).

The failure risk of rock slopes is most commonly mitigated by monitoring the unstable slope. Monitoring is generally the only way of detecting early-warning signals of large, high-risk slope

failures. The monitoring system should be judiciously selected considering the type and size of the slope failure, the deformation rate, data acquisition frequency, required accuracy, and monitoring cost (Travelletti *et al*., 2014).

Slopes can be monitored by various ground-based remote sensing platforms, such as terrestrial optical photogrammetry, terrestrial laser scanning and ground-based synthetic aperture radar interferometry. Such platforms, which have rapidly developed in recent years, allow users to determine the stable and sliding parts of a slope from a safe distance. They also assist in landslide kinematics calculations such as deformation rates, deformation fields, and displacements, by which researchers learn the failure mechanisms of slopes (Casson *et al*., 2005; Delacourt *et al*., 2007; Oppikofer *et al*., 2008; Teza *et al*., 2008; Travelletti *et al*., 2014; Stead and Wolter, 2015).

Recent 3D-laser scanning systems (i.e. LiDAR systems) have revealed the possible locations and times of failure by detecting the precursory movements of a landslide. The LiDAR system scans real objects and their spatial information with a laser light, and recreates their three-dimensional surfaces from the discretely sampled points. The spatial information of a scanned object is stored as a group of x, y, and z coordinates and is exported to external software for creating models or meshes (Jaselskis *et al*., 2005; Royán *et al*., 2013). LiDAR systems are classified into two groups based on their acquiring platform: airborne laser scanning systems (ALSs) and terrestrial laser scanning systems (TLSs). ALSs are generally used for areal data acquisition at spatial resolutions of more than one point per square metre. A TLS gathers more precise measurements over a shorter measuring range, which restricts the study area (Bremer and Sass, 2012; Ozdogan and Deliormanli, 2016). A TLS also needs more processing steps to widen the study area.

LiDAR applications in geotechnical and geological studies have progressed in recent years. Categories of LiDAR-based studies include geometric modelling of 3D rock falls (Abellán *et al*., 2006), estimation of landslide volume (Du and Teng, 2007), estimation of joint orientations (Deliormanli *et al*., 2014), determination of landslide geometry (Dunning *et al*., 2009), and geotechnical mapping of discontinuities (Lato *et al*., 2009). These studies are commonly related to the structural properties and geometrical model of the study area (Hu *et al*., 2012) and require careful attention. In geotechnical investigations, which demand high precision and accuracy, TLS is more preferable than ALS (Bremer and Sass, 2012).

Acquiring reliable data of an active slope is vital for understanding the failure mechanism of that slope. Periodic measurements of the slope surface by a terrestrial laser scanner provide highly accurate data that reveal the development of the slope movement.

However, rock-slope instability can also be triggered by environmental factors such as the subsidence effect of underground production. Rock-slope movements triggered by underground mining operations commonly occur at some time after the abandonment of the mines, leaving no records. Therefore, the effect of underground mining on rock slopes is insufficiently researched and referenced (Szwedzicki, 2003; Zheng *et al*., 2015). Consequently, traditional mine-stability analyses may be inapplicable to elevated open pits and monitoring the slopes of the pit within the influence area of the subsidence will reduce the risk of future slope failure.

This paper evaluates the stability of an open-pit slope above an underground mine and investigates the triggering factors of slope movement. The stability of the studied slope is vital because of the existence of a sludge settling pond beside the pit slope. The stability of the slope was evaluated by means of stereographic-based kinematic analyses to understand if the kinematic conditions of the rock mass caused instability on the slope. Also the studied pit slope was

monitored by the terrestrial Light Detection and Ranging (LiDAR) technique for different four times to reveal the displacements on the slope and determine the change of slope surface angle which can be an effect of underground production.

2. Materials and methods

2.1. TLS measurements in study area

The Soma coal region is located at the west side of Turkey in the Manisa Province (Fig. 1). The coal deposits in the area have been operated by Turkish Coal Enterprises (a governmental company) and various private companies since 1913.

Fig. 1 - Location map of the study area.

According to Inci (1998, 2002) the Soma basin contains Miocene alluvial/fluvial - lacustrine deposits composed of three lignite successions: the lower, middle and upper coal successions. Only the lower coal succession includes an exploitable seam (KM2) with 20 m thick subbituminous lignitic coal between the basal and marlstone units (Tercan *et al*., 2013). Fig. 2 shows the generalised stratigraphic sections of the Soma coal.

The study was carried out in the local pit located in Panel G of the Kartalkaya region, south of Soma City. The KM2 coal seam in this region is inclined by approximately 25-30° and is 20 m thick.

In the open-pit operated by Turkish Coal Enterprises, the base elevation of the coal determined for open-pit production is +200 m. Another coal seam, below +180 m elevation, was planned for underground mining by a private company. Production in underground

mines is usually accomplished by the longwall top caving method. The mining of underground panels was started in November 2013. During the excavation, the surrounding rocks of the underground spaces underwent large deformations that were directly transmitted to the surface, causing a series of subsidence features within 2 months. Subsidence cracks were observed at the top of the south slope of Panel G at the end of January 2014 (Figs. 3a and 3b).

A possible failure at the south slope of Panel G poses a risk to the open-pit coal production. The sludge settling pond located in front of the south slope could also have dramatic consequences. After, subsidence cracks were seen on the surface, both underground and open-pit operations were stopped.

To better understand the rock-slope failure mechanism, the triggering factors of instability, the slope movement, and the stability of the south slope of Panel G were assessed in a kinematical analysis. Also a monitoring study of the same region by TLS, commencing in early 2014, were available for validation.

The orientation of the bedding planes, joints, fault zone and slope face has been revealed in stereographic projection measurements. The observed orientation of the fault in the study area is 90/118 (in dip and dip-direction notation). The measured dip directions of limestone (M3) and marl (M2) layers are (32/190) SW, meaning that the bedding planes dip into the slope. Before the underground mining operation, the south slope of Panel G face was oriented at 40-45/027. Cracks occurred perpendicularly to the bedding plane. The dip direction of the joints is along the base of the south slope on Panel G (85/110). Fig. 4 is the stereographic projection showing the relationships among the bedding planes, joints, fault zone, and south slope of Panel G.

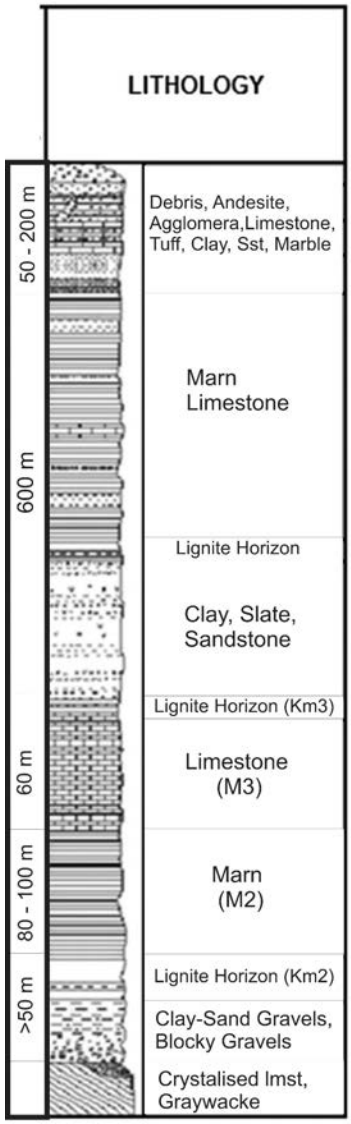

Fig. 2 - Generalised stratigraphic sections of the Soma coal region (from Nebert, 1978).

In rock slope monitoring studies, LiDAR measurements are obstructed by the slope geometry, angle of sight, reflectivity characteristics and vegetation cover of the surface, visibility along the line of sight and scanner-to-slope distance. However, a well-designed field study will detect small slope deformations in TLS data (Kromer *et al*., 2015).

The study area was scanned on 2 February 2014, 17 April 2014, 29 November 2014, and 11 June 2015. The scanning device was a Leica Scanstation 2 high-definition surveying (HDS) instrument, providing almost complete coverage of the southern slopes where surface changes are expected (see Fig. 5). The technical features of the device are listed in Table 1.

The viewing and processing of high-definition point clouds are intensive tasks requiring powerful software. In the present study, the point clouds were scanned and managed by Cyclone V8.0, a scanning and point-processing software developed by Leica.

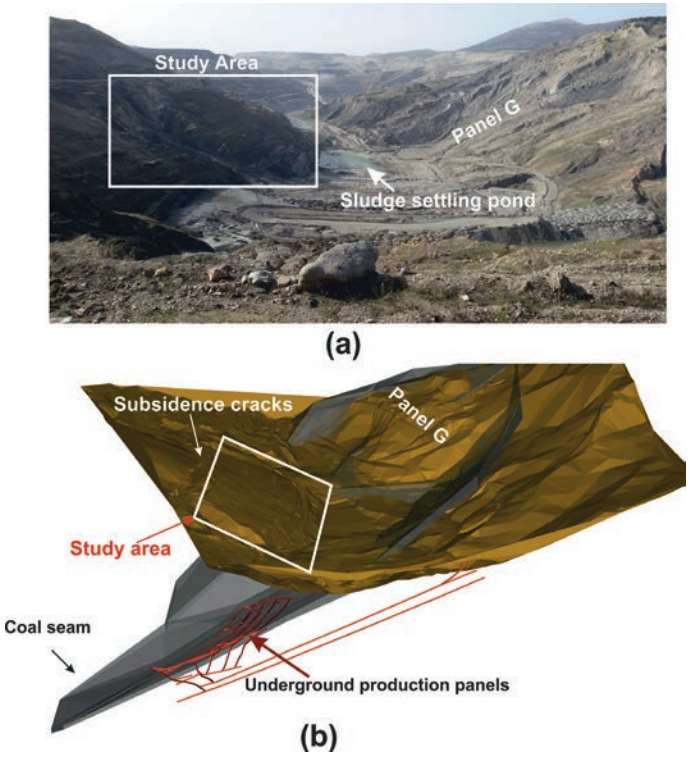

Fig. 3 - Study area: a) general view of basin and b) 3D model.

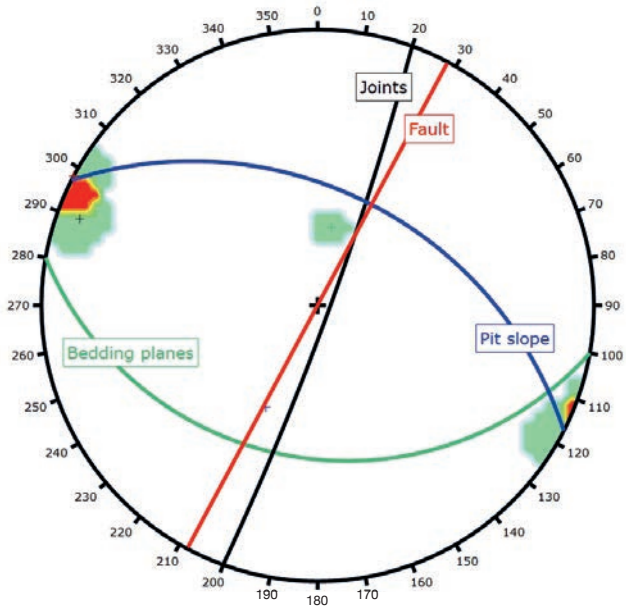

Fig. 4 - Stereographic projection of the bedding planes, joints, fault zone and south slope of Panel G of the study area (blue arc: pit slope: green arc: bedding plane; red line: fault; black line: joints).

TLS data acquisition involves the following four steps:
- planning of scan area;
- data acquisition;
- data processing (registration and merging data);
- evaluation of data.

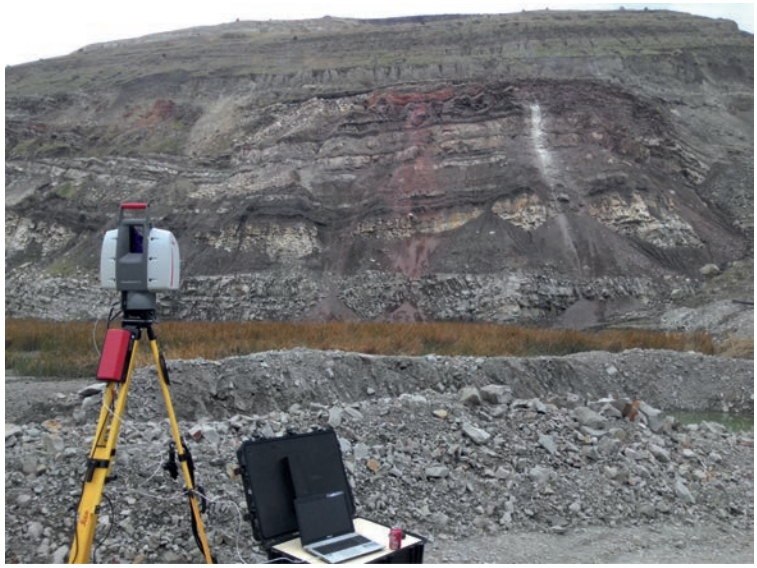

Fig. 5 - General view of studied pit slope.

Table 1 - Specifications of Leica Station 2.

Instrument type	Pulsed, dual-axis compensated, very-high speed laser scanner, with survey grade accuracy, range, and field-of-view.
User interface	Notebook or Tablet PC.
Accuracy of single measurement	Position*: 6 mm. Distance*: 4 mm. Angle (horizontal/vertical): 60 µrad/60 µrad.
Laser spot size	0-50 m: 4 mm (FWHH-based); 6 mm (Gaussian-based).
Target acquisition	2 mm std. deviation.
Laser scanning system	Range: 300 m @ 90 %; 134 m @ 18 % albedo. Scan rate: Maximum instantaneous: up to 50,000 points/sec. Scan density: < 1 mm max, through full range; fully selectable horizontal and vertical spacing; single point dwell capability.

* 1σ at 50 m range

2.2. Methodology of TLS measurements

Owing to the topographical structure of the slope, varying scan distance and varying incidence angle of the laser beam, the point-cloud data taken from the scan area are heterogeneously distributed. Therefore, to maximise the data coverage and efficiency, the scanning station must be optimally located to collect as much data as possible from the areas of interest. In this study, three on-site stations along the slope (Fig. 6) were selected to reduce the shadow-masked zone and enlarge the acquisition area.

The data acquisition and processing step determines the scan resolution, registers and merges the data and implements the georeferencing. In the present study, the data were processed by Cylone V8.0 software. The TLS data were resolved to 0.1×0.1 m^2 (horizontal × vertical resolution)

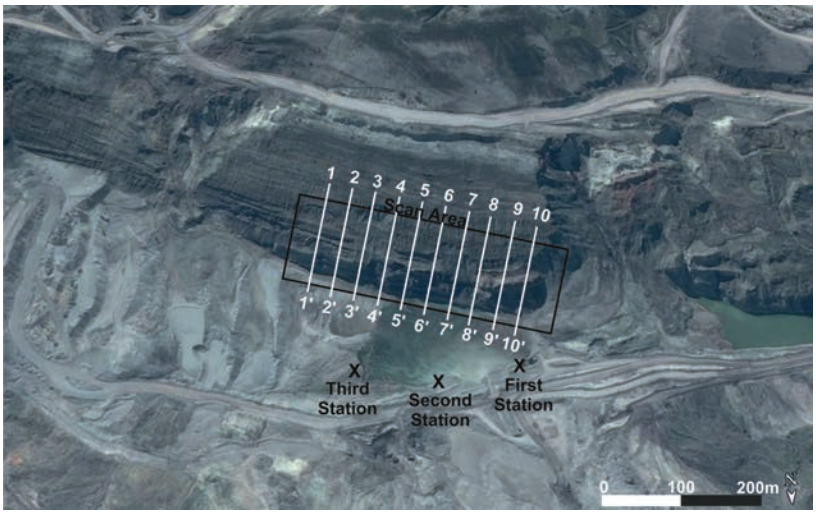

Fig. 6 - Locations of stations and transects.

at 300 m from the scanned surface. The maximum distance of the TLS acquisition was 200 m from the south slope of Panel G. The monitored slope was free of vegetation. The point cloud in each scan was registered, merged and georeferenced with respect to three HDS targets, which were individually scanned after scanning the slope. The 300-m vertical and horizontal resolutions of the target scans were 0.02 and 0.02 m, respectively, enabling automatic detection of targets in the point cloud and perfect registration of the point clouds. The root mean square error of the registration varied between 2.0 and 3.8 mm.

To acquire the coordinates of the HDS targets and georeference the merged point cloud, we employed the real-time kinematic mode of the Leica C25 global positioning system. The processed and cleaned point-cloud data of the scan area are presented in panels a and b of Fig. 7, respectively. In the cleaned image, data beyond the study area or absent in at least two scans were removed.

2.3. Methodology of kinematic analysis for rock-slope failure

Rock-slope failure is broadly classified as planar, wedge and toppling (Wyllie and Mah, 2004). For planar rock-slope failure, the surface must meet the following five geometrical criteria: i) the plane on which sliding occurs must strike the slope face in the sliding direction (within approx. ±20°); ii) a release surface must be available for characterising the lateral slide boundaries; iii) the sliding plane must 'outcrop' in the slope face; iv) the dip of the sliding plane must exceed the friction angle and v) the upper end of the sliding plane must intersect the upper slope, or end in a tension crack (Hoek and Bray, 1981).

Wedge failure is similar to planar failure, but occurs along the intersection line of two discontinuities. For a kinematically acceptable wedge failure, the intersection line must satisfy the following criteria: i) the dip of the slope must exceed the dip of the intersection line of the two discontinuity planes forming the wedge; ii) the line of intersection must 'outcrop' on the slope face; iii) the intersection line should dip sufficiently to reach the yield strength of both planes and iv) the upper end of the intersection line must intersect the upper slope, or terminate in a tension crack.

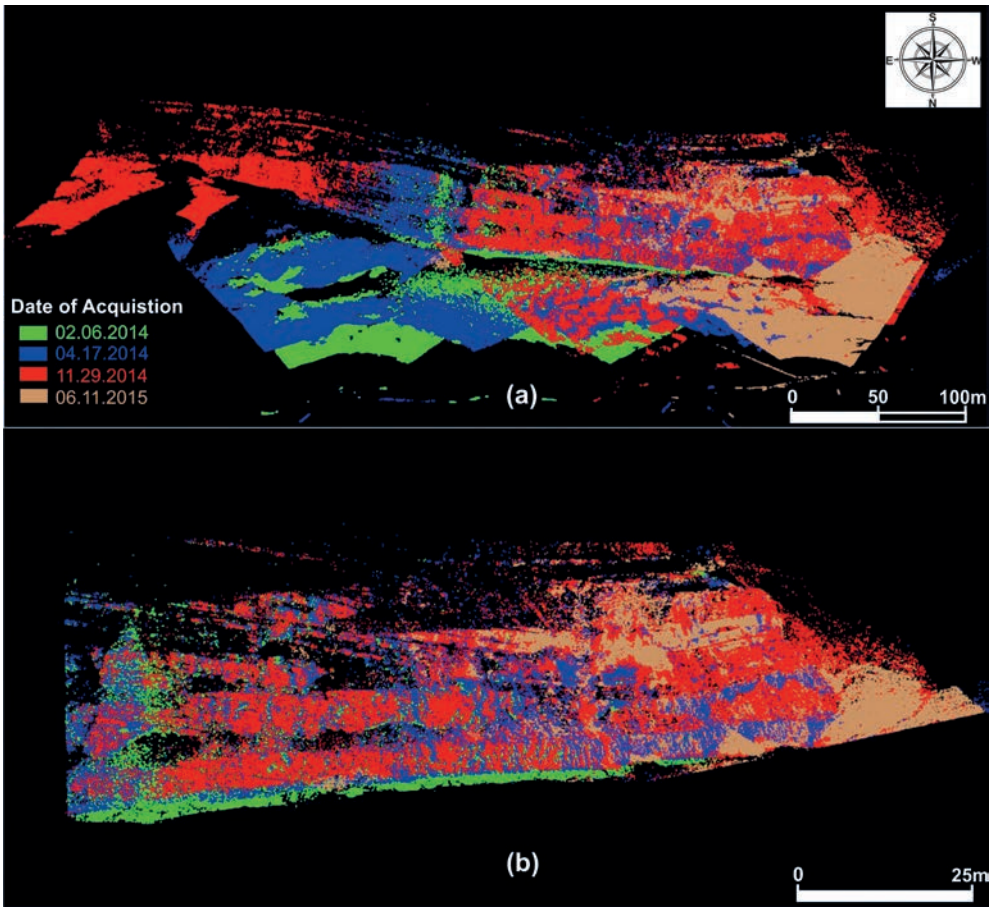

Fig. 7 - Point-cloud data acquired by TLS measurements from studied area (a: the scan area; b: the studied scene).

A toppling failure in the slope occurs under the following conditions: i) discontinuities parallel to the slope face (within ±30°) dipping steeply into the slope face; ii) interlayer slip movement; iii) the angle of the direction of the applied compression exceeds the friction angle Φ_j between two layers, relative to the normal to the layers (Goodman and Bray, 1976), and iv) (for interlayer slippage) the normals are inclined less steeply than a line inclined at Φ_j above the plane of the slope. If the layers are dipped by an amount σ, then a slope inclined at α degrees from the horizontal can topple if $(90 - \sigma) + \Phi_j < \alpha$.

Rock-slope stability can be assessed by various analytical methods (Hoek and Bray, 1981; Goodman, 1989; Pettifer and Fookes, 1994), including kinematical, limit equilibrium, and numerical analyses. Kinematic analysis is useful for defining planar, wedge and toppling failure modes and is especially popular in structural geology and rock mechanics. A kinematic analysis determines the slope failure mechanism using stereographic-based kinematic methods, which have been summarised in numerous publications (Richards *et al*., 1978; Priest; 1980; Hoek and Bray, 1981; Wyllie and Mah, 2004). However, kinematic analysis may not adequately account for discontinuity persistence, spacing and discontinuity shear strength. To reduce these limitations, stereographic kinematic analyses should be ground-truthed by field investigations. The field study

first assesses the effects of major discrete structures, such as faults/shear zones and persistent bedding planes, on the slope stability. In the second step, it incorporates the instability mechanisms associated with the joint sets.

3. Results of slope monitoring and stability evaluation

In this study, the slope failure was defined in a kinematic analysis of discontinuity orientation data. The presence of slope instability and validity of the kinematic analysis results were determined in comparisons with TLS point-cloud data taken on various dates.

3.1. Kinematic stability analysis

Given the slope geometry and discontinuity orientation, a kinematic analysis determines whether and where a particular instability mechanism is kinematically possible (Goodman and Bray, 1976; Hoek and Bray, 1981; Matheson, 1989; Hudson and Harrison, 1997). The kinematic analysis investigates various instability mechanisms: plane failure, wedge failure, block toppling, and flexural toppling. All kinematic stability analyses were executed on stereographic projection images using Dips 6.0 software (Rocscience Inc., 2014).

Before the underground mining operation in the study area, the slope orientation was 40-45/027. The measured orientations of the main discontinuities in the field were given in subsection 2.1. The analysis results are displayed in Figs. 8 to 11. In all analyses, the friction angle of the friction cone was approximately 55°.

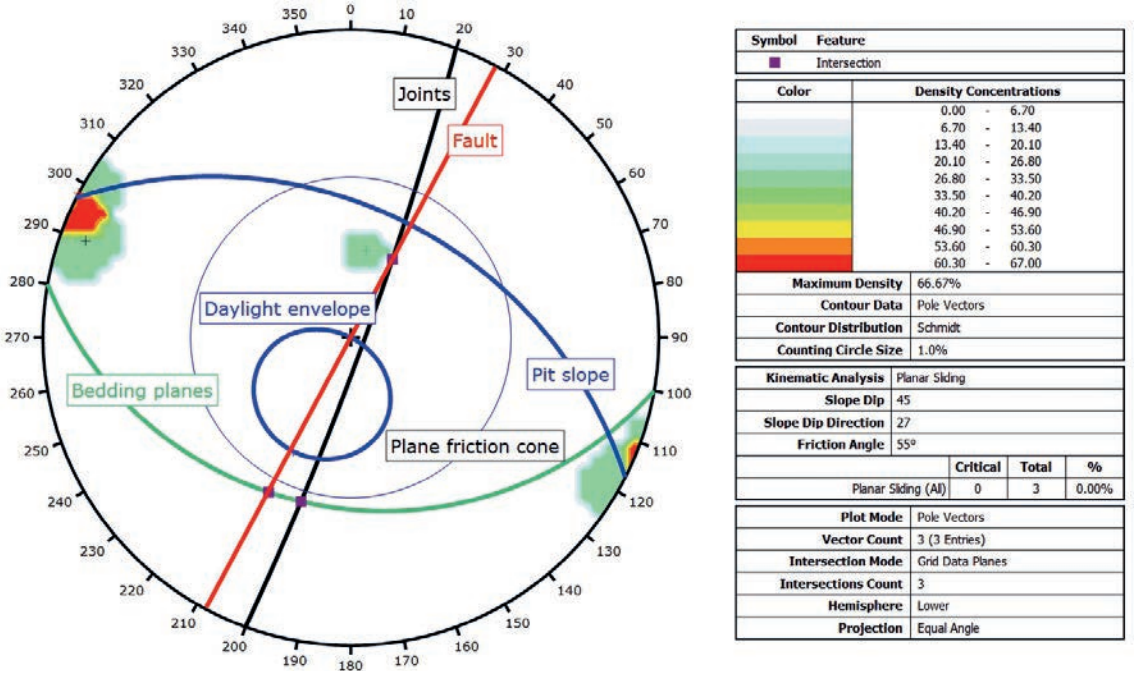

Symbol	Feature
■	Intersection

Color	Density Concentrations
	0.00 - 6.70
	6.70 - 13.40
	13.40 - 20.10
	20.10 - 26.80
	26.80 - 33.50
	33.50 - 40.20
	40.20 - 46.90
	46.90 - 53.60
	53.60 - 60.30
	60.30 - 67.00

Maximum Density	66.67%
Contour Data	Pole Vectors
Contour Distribution	Schmidt
Counting Circle Size	1.0%

Kinematic Analysis	Planar Sliding
Slope Dip	45
Slope Dip Direction	27
Friction Angle	55°

	Critical	Total	%
Planar Sliding (All)	0	3	0.00%

Plot Mode	Pole Vectors
Vector Count	3 (3 Entries)
Intersection Mode	Grid Data Planes
Intersections Count	3
Hemisphere	Lower
Projection	Equal Angle

Fig. 8 - Planar-sliding analysis of the slope face before the underground mining operation. There is no possibility of planar sliding (blue arc: pit slope; green arc: bedding plane; red line: fault; black line: joints; blue circle: daylight envelope; grey circle: plane friction cone).

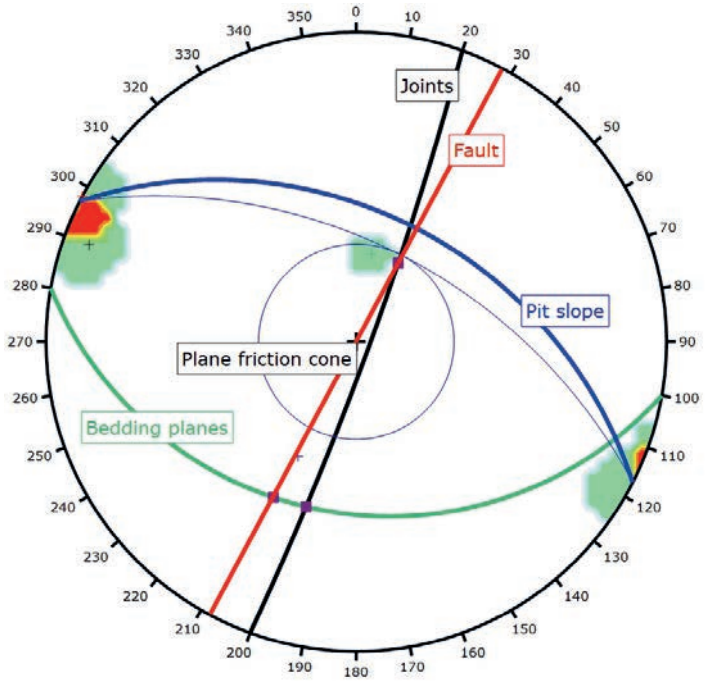

Symbol	Feature
	Critical Intersection
	Intersection

Color	Density Concentrations
	0.00 - 6.70
	6.70 - 13.40
	13.40 - 20.10
	20.10 - 26.80
	26.80 - 33.50
	33.50 - 40.20
	40.20 - 46.90
	46.90 - 53.60
	53.60 - 60.30
	60.30 - 67.00

Maximum Density	66.67%
Contour Data	Pole Vectors
Contour Distribution	Schmidt
Counting Circle Size	1.0%

Kinematic Analysis	Wedge Sliding
Slope Dip	45
Slope Dip Direction	27
Friction Angle	55°

	Critical	Total	%
Wedge Sliding	0	3	0.00%

Plot Mode	Pole Vectors
Vector Count	3 (3 Entries)
Intersection Mode	Grid Data Planes
Intersections Count	3
Hemisphere	Lower
Projection	Equal Angle

Fig. 9 - Wedge sliding analysis of the slope face before the underground mining operation. There is no possibility of wedge sliding (blue arc: pit slope; green arc: bedding plane; red line: fault; black line: joints; grey circle: plane friction cone).

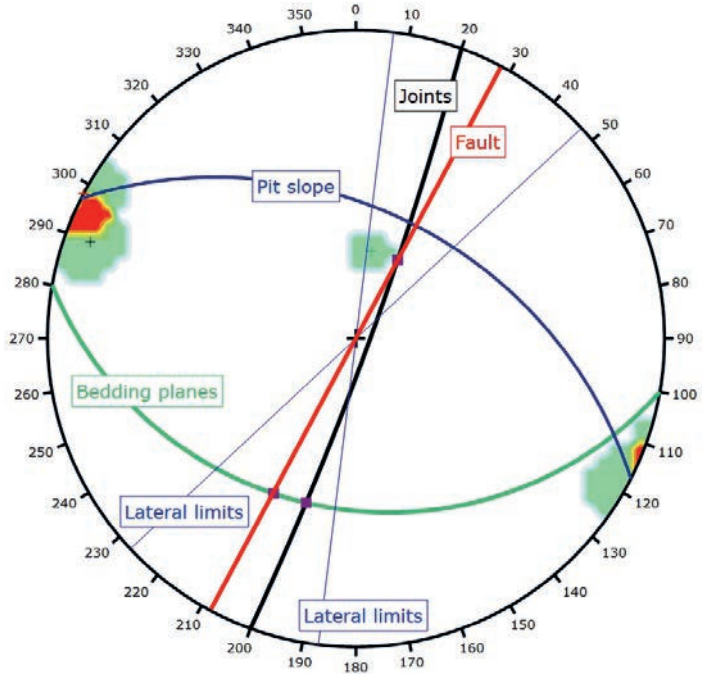

Symbol	Feature
	Intersection

Color	Density Concentrations
	0.00 - 6.70
	6.70 - 13.40
	13.40 - 20.10
	20.10 - 26.80
	26.80 - 33.50
	33.50 - 40.20
	40.20 - 46.90
	46.90 - 53.60
	53.60 - 60.30
	60.30 - 67.00

Maximum Density	66.67%
Contour Data	Pole Vectors
Contour Distribution	Schmidt
Counting Circle Size	1.0%

Kinematic Analysis	Flexural Toppling
Slope Dip	45
Slope Dip Direction	27
Friction Angle	55°
Lateral Limits	20°

	Critical	Total	%
Flexural Toppling (Al)	0	3	0.00%

Plot Mode	Pole Vectors
Vector Count	3 (3 Entries)
Intersection Mode	Grid Data Planes
Intersections Count	3
Hemisphere	Lower
Projection	Equal Angle

Fig. 10 - Flexural toppling analysis of the slope face before the underground mining operation. There is no possibility of flexural toppling (blue arc: pit slope; green arc: bedding plane; red line: fault; black line: joints; light blue lines: lateral limits).

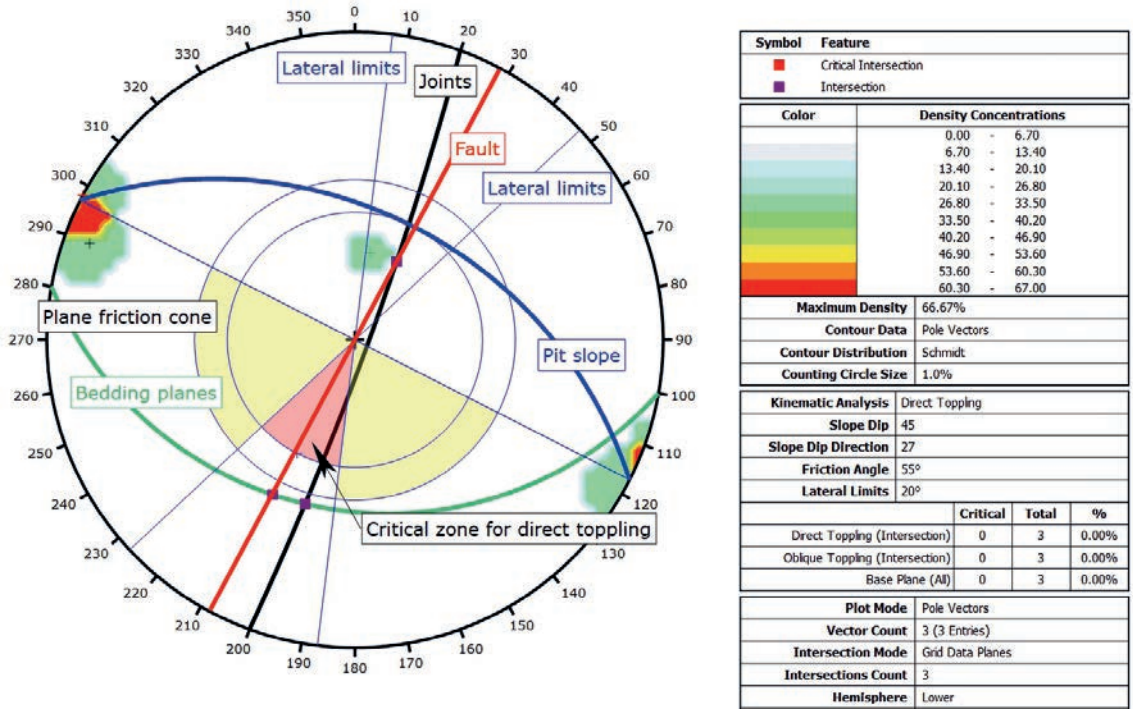

Symbol	Feature
	Critical Intersection
	Intersection

Color	Density Concentrations
	0.00 - 6.70
	6.70 - 13.40
	13.40 - 20.10
	20.10 - 26.80
	26.80 - 33.50
	33.50 - 40.20
	40.20 - 46.90
	46.90 - 53.60
	53.60 - 60.30
	60.30 - 67.00

Maximum Density	66.67%
Contour Data	Pole Vectors
Contour Distribution	Schmidt
Counting Circle Size	1.0%

Kinematic Analysis	Direct Toppling
Slope Dip	45
Slope Dip Direction	27
Friction Angle	55°
Lateral Limits	20°

	Critical	Total	%
Direct Toppling (Intersection)	0	3	0.00%
Oblique Toppling (Intersection)	0	3	0.00%
Base Plane (All)	0	3	0.00%

Plot Mode	Pole Vectors
Vector Count	3 (3 Entries)
Intersection Mode	Grid Data Planes
Intersections Count	3
Hemisphere	Lower

Fig. 11 - Direct toppling analysis of the slope face before the underground mining operation. There is no possibility of direct toppling (blue arc: pit slope; green arc: bedding plane; red line: fault; black line: joints; light blue lines: lateral limits).

The critical zone (crescent-shaped) created by the pole friction circle and the Daylight Envelope surrounds the region of planar failure. Any poles in the zone symbolise planes that can slide the crescent-shaped zone for planar failure are described. The results of the planar sliding kinematic analysis are given in Fig. 8. The results confirm no possibility of planar failure in the slope.

The crescent-shaped area is a main critical region for wedge failure. The zone is outside the slope plane and inside the plane friction cone. Any intersection points in the main critical zone characterise wedges which can slide. The area between a plane inclined at the friction angle and the slope plane is defined as secondary critical region. Any critical intersections mean in these regions symbolise wedges that slide on one discontinuity plane. In this zone, the intersections are essentially inclined at less than the friction angle. However, sliding is able to place on a single discontinuity plane as a dip vector greater than the friction angle. The wedge sliding kinematic analysis results are shown in Fig. 9. The results show that no possibility of wedge failure in the slope.

The critical zone for flexural toppling is defined between the lateral limits, stereonet outline, and the slip limit plane. Any poles in the critical zone represent a flexural toppling risk (Goodman, 1980). Depending on the flexural toppling analysis the results in Fig. 10 show that there is no significant risk of flexural toppling.

Direct toppling analysis was described in Hudson and Harrison (1997). Direct toppling differs from flexural toppling for two different basic features:

- two discontinuity sets intersect to create intersection lines dipping into the slope that can create separated blocks;

- a third discontinuity set in the horizontal planes behaves as release planes for the separated blocks.

The results of the direct toppling analysis are displayed in Fig 11. The results show that there is no possibility of direct toppling failure.

3.2. Results of terrestrial laser scanner measurements

After commencement of the underground mining operation, subsidence cracks were seen on the slope surface, and the beginnings of failure appeared on the slope face. The presence of slope instability was determined from displacement measurements of transects using Cyclone V8.0 software. The section lines were compared with those of an initial reference section. The negative and positive displacements (relative to the reference) indicate pouring of material and advancement of the slope surface, respectively (Fig. 12). The transect analysis determines the farthest vertical distance between the oldest and latest point data. The point-cloud data of lines 6 and 8 of the cross-section are missing in the first scan, due to the scanning angle. For the same reason, the point-cloud data in lines 1-3 and line 5 of the cross-section are missing from the scan taken on 6 November 2015.

Significant slope deformation is observed in the transect analyses, but is absent in the kinematic analyses. Therefore, underground production was solely responsible for the slope instability in the study area. The original slope dip angle was 40-45 degrees. After the underground mining

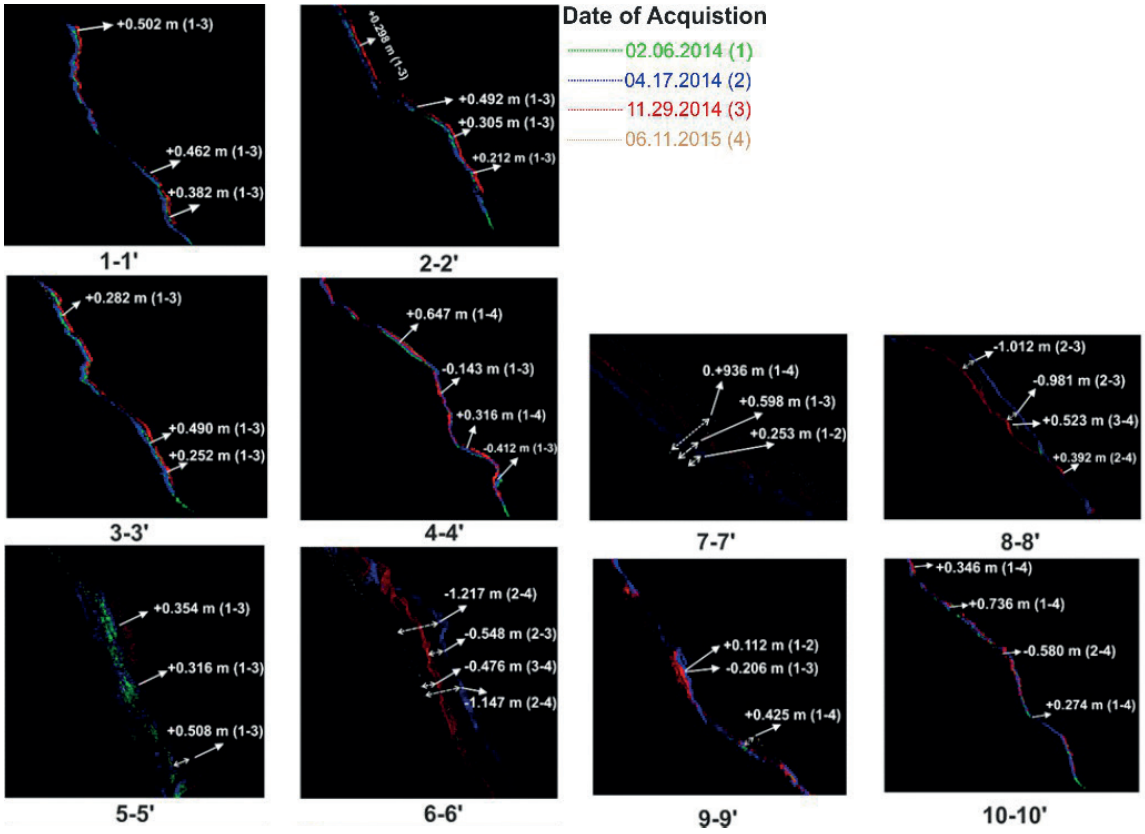

Fig. 12 - Significant displacements determined by transect analysis.

operation, the slope was deformed by subsidence. So secondary slope faces occurred on the initial slope face. These secondary surfaces are displayed in Fig. 12. The angle of the secondary surfaces varies between 45 and 90 degrees. These results are confirmed by the slope angle analysis using point-cloud data (Figs. 17 to 20).

The possible unstable slope-surface angles were determined by increasing the slope surface angle of the stereographic projection. According to the results, the critical slope-surface angle value is ~58°. Plane failure, wedge failure, block toppling and flexural toppling occurred at angles between 58 and 90° on the slope surface. Within this range, the whole kinematic stability analysis was realised from the stereographic projections using maximum slope angles degree 90 (Figs. 13 to 16).

The planar sliding kinematic analysis results are given in Fig. 13. Two intersections are contained in the critical zone. It can be seen that the probability of planar sliding is about 66.67% for this condition.

According to the wedge kinematic analysis results in Fig. 14, an intersection point is shown in the primary critical zone for wedge sliding. The percentage of critical intersections is actually not very low (about 33%) in the critical zone. Therefore, wedge sliding is a concern for this slope orientation.

Flexural toppling analysis results are given in the legend of Fig 15. It is clear that there is no intersection in the critical zone. So there is no significant risk of flexural toppling.

Direct toppling analysis results are given Fig 16. The results show that two critical intersections in critical zone for direct toppling. It means that direct toppling occurs on slope face. The direct toppling probability is nearly 67%.

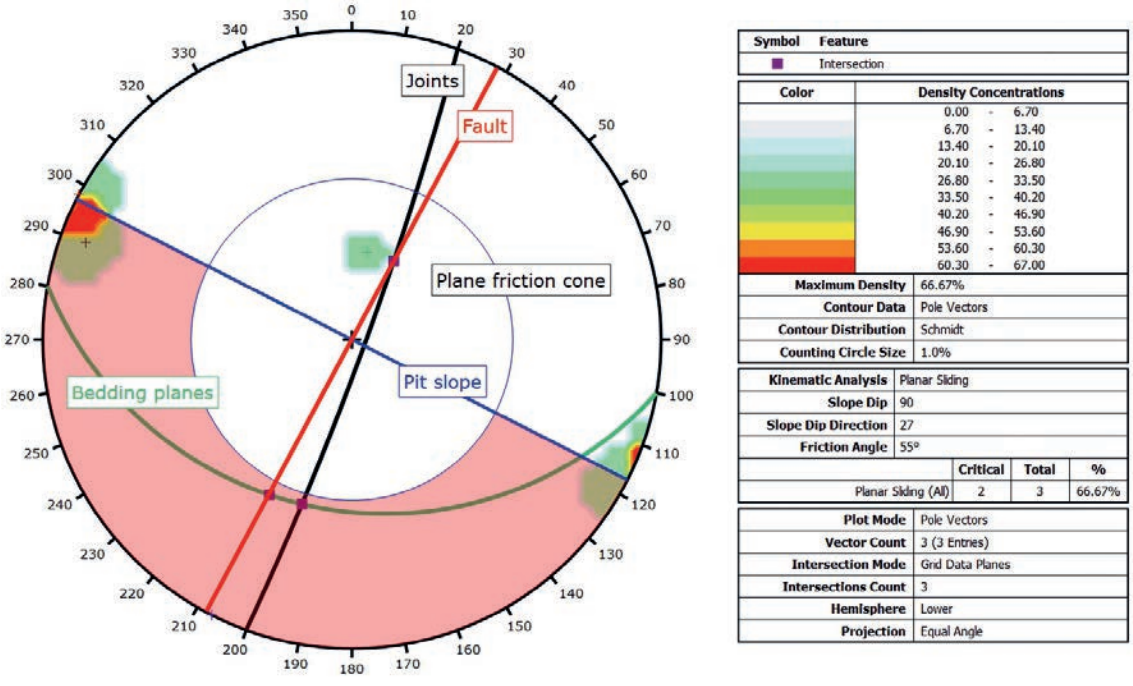

Symbol	Feature
■	Intersection

Color	Density Concentrations
	0.00 - 6.70
	6.70 - 13.40
	13.40 - 20.10
	20.10 - 26.80
	26.80 - 33.50
	33.50 - 40.20
	40.20 - 46.90
	46.90 - 53.60
	53.60 - 60.30
	60.30 - 67.00

Maximum Density	66.67%
Contour Data	Pole Vectors
Contour Distribution	Schmidt
Counting Circle Size	1.0%

Kinematic Analysis	Planar Sliding
Slope Dip	90
Slope Dip Direction	27
Friction Angle	55°

	Critical	Total	%
Planar Sliding (All)	2	3	66.67%

Plot Mode	Pole Vectors
Vector Count	3 (3 Entries)
Intersection Mode	Grid Data Planes
Intersections Count	3
Hemisphere	Lower
Projection	Equal Angle

Fig. 13 - Planar-sliding analysis after the underground mining operation, showing two critical possibilities of planar sliding at 90° slope angle (blue arc: pit slope; green arc: bedding plane; red line: fault; black line: joints; grey circle: plane friction cone).

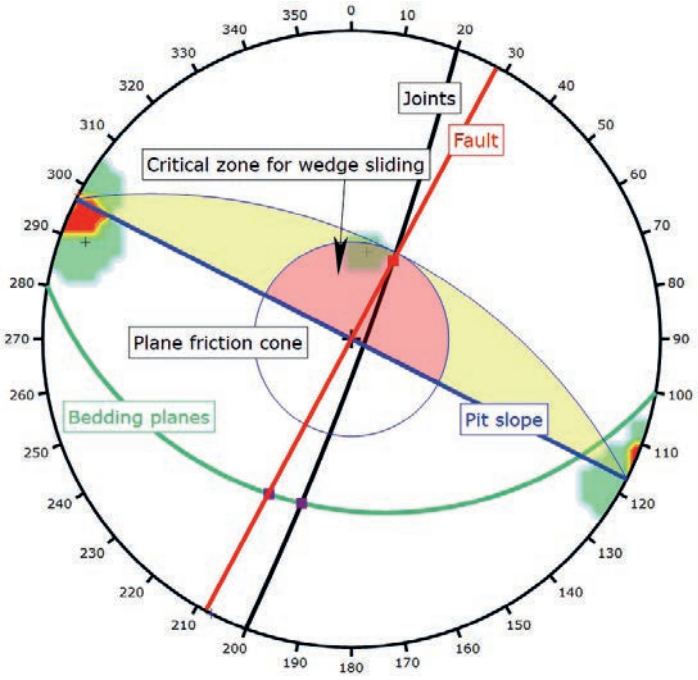

Symbol	Feature
■	Critical Intersection
■	Intersection

Color	Density Concentrations
	0.00 - 6.70
	6.70 - 13.40
	13.40 - 20.10
	20.10 - 26.80
	26.80 - 33.50
	33.50 - 40.20
	40.20 - 46.90
	46.90 - 53.60
	53.60 - 60.30
	60.30 - 67.00

Maximum Density	66.67%
Contour Data	Pole Vectors
Contour Distribution	Schmidt
Counting Circle Size	1.0%

Kinematic Analysis	Wedge Sliding
Slope Dip	90
Slope Dip Direction	27
Friction Angle	55°

	Critical	Total	%
Wedge Sliding	1	3	33.33%

Plot Mode	Pole Vectors
Vector Count	3 (3 Entries)
Intersection Mode	Grid Data Planes
Intersections Count	3
Hemisphere	Lower
Projection	Equal Angle

Fig. 14 - Wedge sliding analysis after the underground mining operation, showing one critical possibility of wedge sliding at 58-90° slope angle (blue arc: pit slope; green arc: bedding plane; red line: fault; black line: joints; grey circle: plane friction cone).

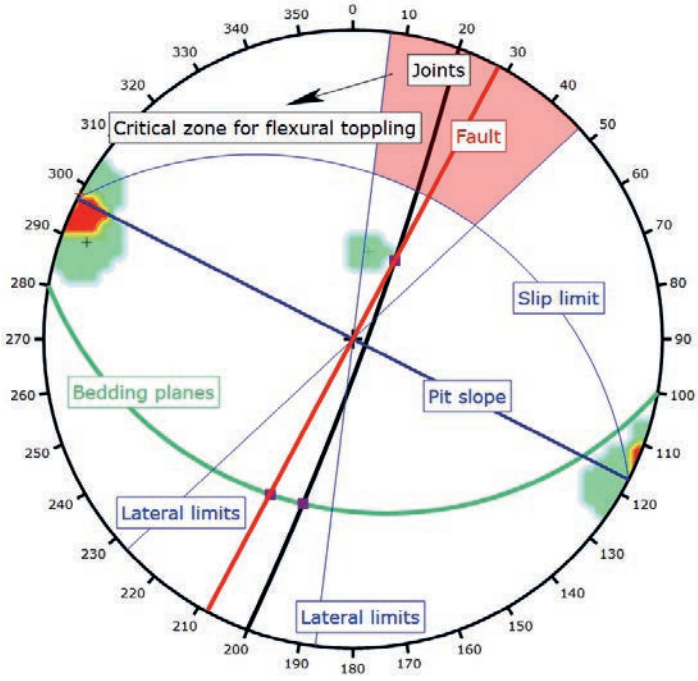

Symbol	Feature
■	Intersection

Color	Density Concentrations
	0.00 - 6.70
	6.70 - 13.40
	13.40 - 20.10
	20.10 - 26.80
	26.80 - 33.50
	33.50 - 40.20
	40.20 - 46.90
	46.90 - 53.60
	53.60 - 60.30
	60.30 - 67.00

Maximum Density	66.67%
Contour Data	Pole Vectors
Contour Distribution	Schmidt
Counting Circle Size	1.0%

Kinematic Analysis	Flexural Toppling
Slope Dip	90
Slope Dip Direction	27
Friction Angle	55°
Lateral Limits	20°

	Critical	Total	%
Flexural Toppling (All)	0	3	0.00%

Plot Mode	Pole Vectors
Vector Count	3 (3 Entries)
Intersection Mode	Grid Data Planes
Intersections Count	3
Hemisphere	Lower
Projection	Equal Angle

Fig. 15 - Flexural toppling analysis after the underground mining operation. There is no critical possibility of flexural toppling at 58-90° slope angle (blue arc: pit slope; green arc: bedding plane, light blue arc: slip limit, red line: fault, black line: joints; light blue lines: lateral limits).

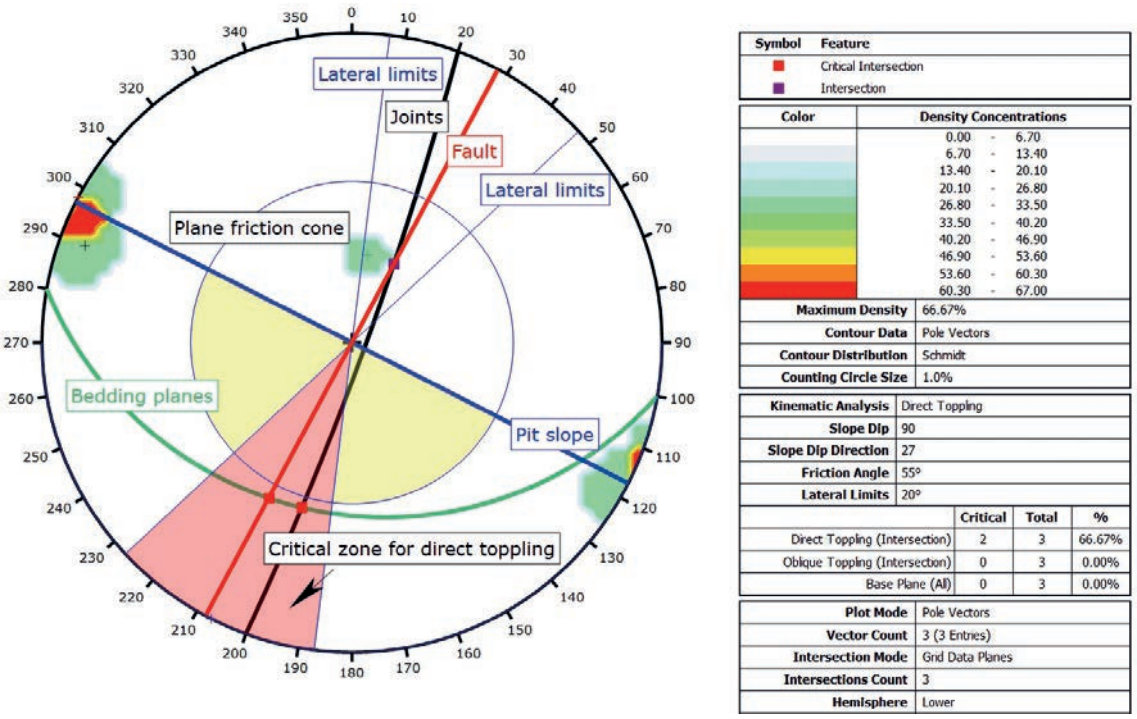

Symbol	Feature
■	Critical Intersection
■	Intersection

Color	Density Concentrations
	0.00 - 6.70
	6.70 - 13.40
	13.40 - 20.10
	20.10 - 26.80
	26.80 - 33.50
	33.50 - 40.20
	40.20 - 46.90
	46.90 - 53.60
	53.60 - 60.30
	60.30 - 67.00

Maximum Density	66.67%
Contour Data	Pole Vectors
Contour Distribution	Schmidt
Counting Circle Size	1.0%

Kinematic Analysis	Direct Toppling
Slope Dip	90
Slope Dip Direction	27
Friction Angle	55°
Lateral Limits	20°

	Critical	Total	%
Direct Toppling (Intersection)	2	3	66.67%
Oblique Toppling (Intersection)	0	3	0.00%
Base Plane (All)	0	3	0.00%

Plot Mode	Pole Vectors
Vector Count	3 (3 Entries)
Intersection Mode	Grid Data Planes
Intersections Count	3
Hemisphere	Lower

Fig. 16 - Direct toppling analysis after the underground mining operation, showing two critical possibilities of direct toppling at 58-90° slope angle (blue arc: pit slope, green arc: bedding plane, red line: fault, black line: joints, light blue lines: lateral limits).

The results confirm that no possibility of flexural toppling in the slope face, although plane, wedge and block-toppling failures are possible. These three failure modes (block-toppling, planar, and wedge) are identified in the slope face, and are indicated as the red regions in Figs. 17 to 20.

4. Discussion

Once the instability conditions were determined by kinematical analyses, the variation of the slope-surface angle triggered by underground production was revealed in the models created from the TLS measurements. The model study was carried out using a 3D Reshaper point-cloud and mesh-processing software. Slope analysis reveals the slopes of a mesh or a point cloud. Each point in the cloud or mesh vertex is assigned an inspection value that depends on the angle between the local normal of the surface and the horizontal. The slope-angle variations on each scanning date are shown in Figs. 17 to 20. Where the surface angle exceeds 58°, the surface is deemed to be at high failure risk.

According to the results of the analyses, the pit slope has moved to the front of the slope. Time-dependent analyses show the continuous repetition of this movement. Therefore, after each scan, the red zone area either decreases or increases although expected to increase.

The direction of movement of failure surfaces in an open-pit slope was determined as a dip direction without manual measurement using three-point data method. The method is well known

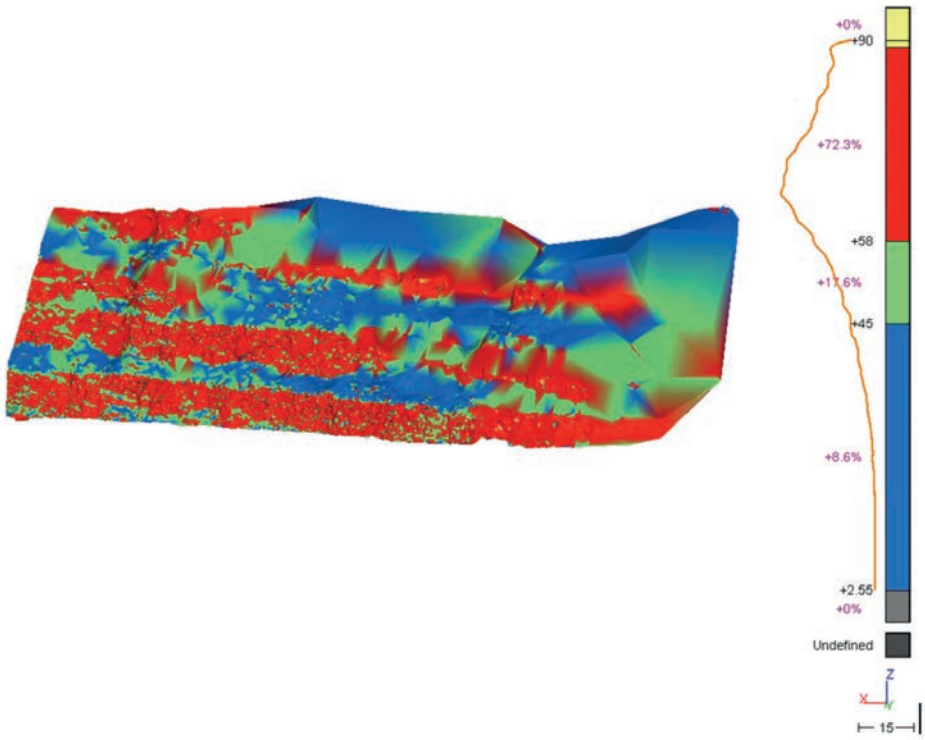

Fig. 17 - Distribution of slope surface angles determined from point cloud data after first TLS scan on 2 February 2014. Red regions have failure risk.

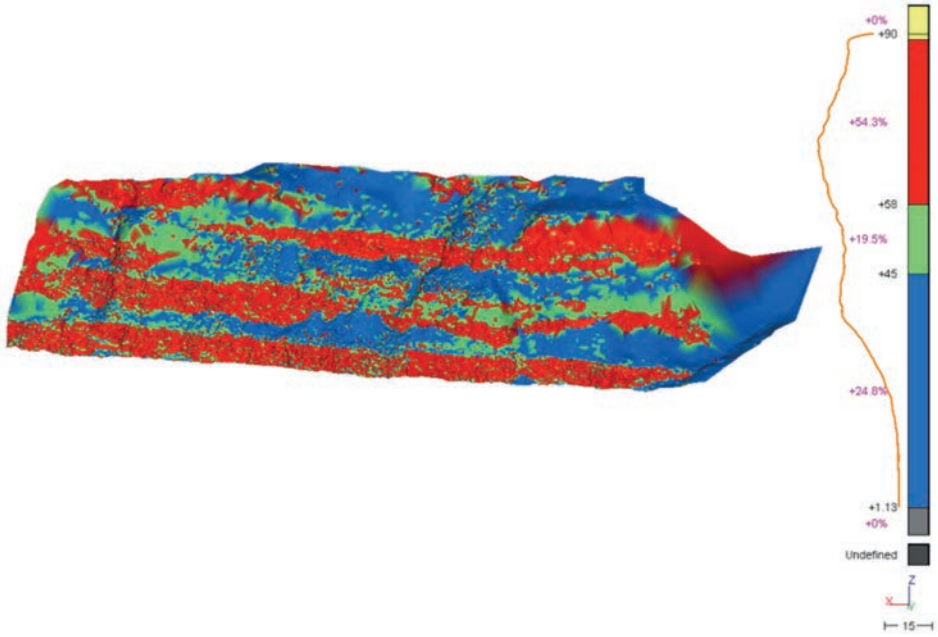

Fig. 18 - Distribution of slope surface angles determined from point cloud data after second TLS scan on 17 April 2014. Red regions have failure risk.

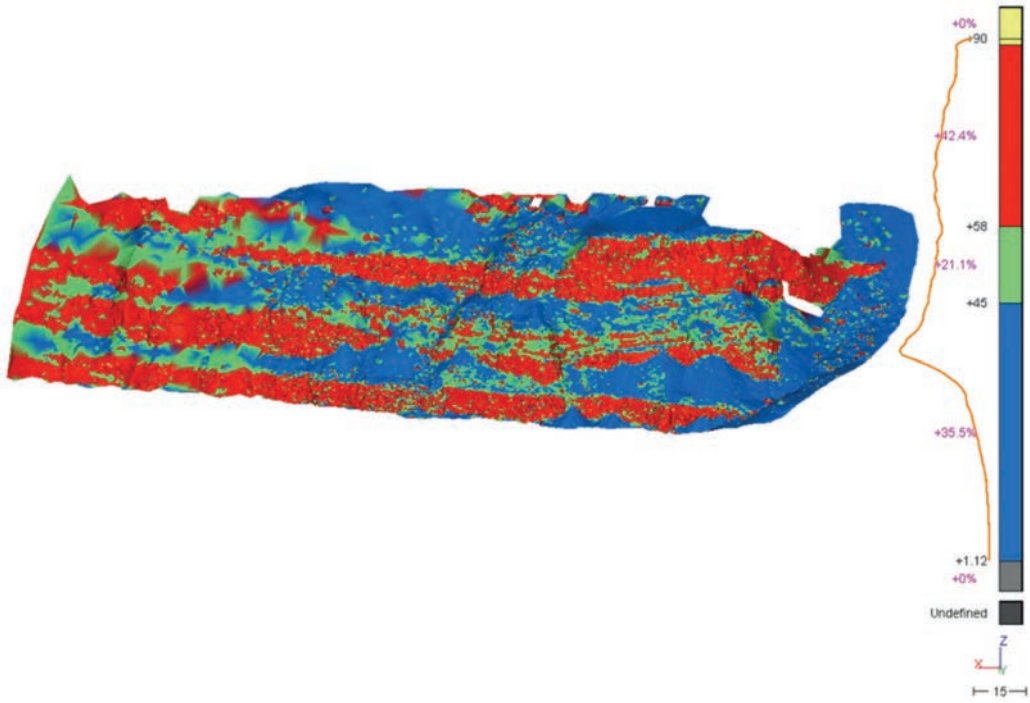

Fig. 19 - Distribution of slope surface angles determined from point cloud data after third TLS scan on 29 November 2014. Red regions have failure risk.

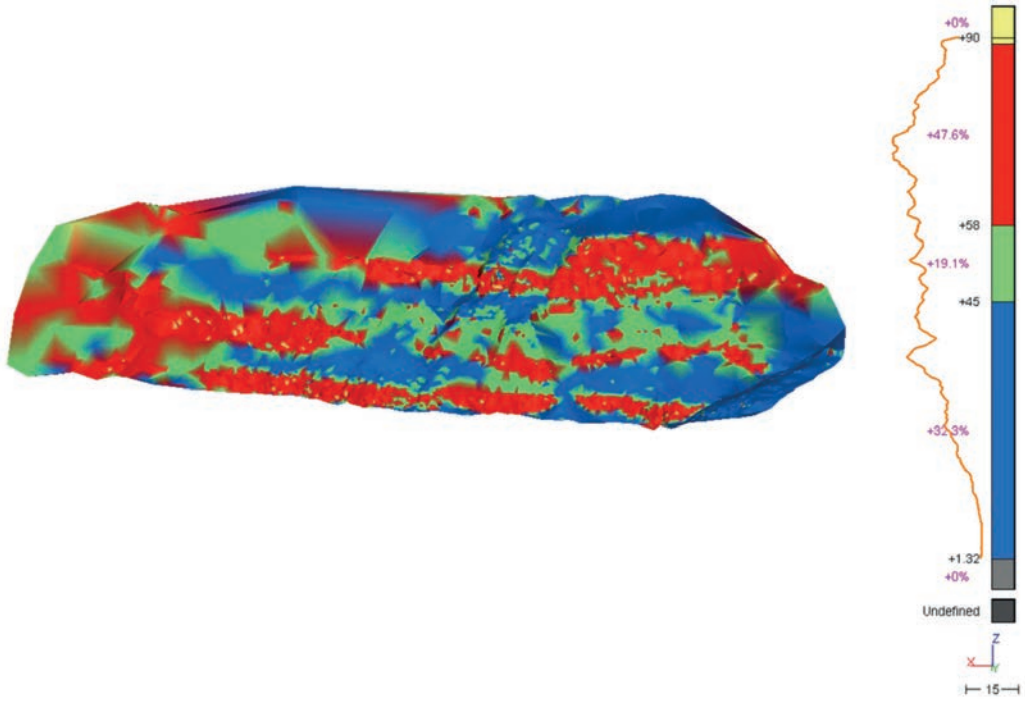

Fig. 20 - Distribution of slope surface angles determined from point cloud data after fourth TLS scan on 11 June 2015. Red regions have failure risk data.

and is based on an analytical expression that can be easily calculated. The definition of three-dimensions of the three non-collinear points is given in Fig. 21.

Using the Cyclone software viewer module, three individual points obtained from point cloud data on the slope face were selected for each TLS measurement. The calculated results show that the average of movement of failure surfaces dip direction is about 014 for the study area. Prior to the underground mining operation, the dip direction of slope face was 027. In other words, the slope direction has moved to the north.

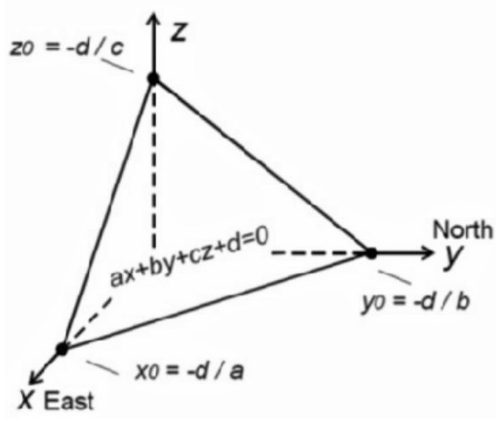

Fig. 21 - The equation of a plane in linear-coefficient for three-point problem.

5. Conclusions

Past studies confirmed that precursory activities can be monitored before the occurrence of slope failure (Kaiser, 1993; Szwedzicki, 2003; Hu *et al*., 2012). Failure can be prevented by an appropriate monitoring system.

In this work, the slope failures and displacements of subsidence-induced slope movements were measured by a simple approach. This study shows that the rock slopes above an underground mine can be unstable even when the surface-measured kinematical conditions indicate stability. Underground production changes the slope-surface angle, and, hence, the current kinematical conditions of the slope. The potential end result is failure.

In the present study, failure threat due to slope deformation is potentially exacerbated by the sludge settling pond located in front of the open-pit slope. Detailed analyses showed that the pit slope has deformed to the front of the slope, broken away, and fallen into the sludge settling pond. Time-dependent analyses confirmed the continuous repetition of this movement. On the other hand, the kinematic analyses proved that the kinematic stability conditions are not responsible from instability of pit slope and slope deformation was triggered by underground production. Therefore, the slope failure in the study area is a complex combination of two or more failure types. Consequently, the slope movements are small and the failures are non-critical, posing no risk to the sludge settling pond. Clearly, these slope movements are the results of underground mining.

The results of this study show that regular examination and systematic monitoring of the slope failures are vital for early detection of failure and any associated hazards. It is possible to obtain data quickly and accurately using TLS.

3D modelling and deformation of slope surfaces can be easily revealed using these data. TLS measurements also provide data in kinematic stability analysis. It is clear that TLS techniques are highly reliable systems for monitoring and analysing the slope stability in open-pit mine.

Acknowledgements. This research was supported by Dokuz Eylul University, Engineering Faculty (Project n. 2012 KB FEN 61 and Project n. 2013 KB FEN 010), and Dokuz Eylul University, the Graduate School of Natural and Applied Sciences (Project n. 2011 KB FEN 12).

REFERENCES

Abellán A., Vilaplana J.M. and Martínez J.; 2006: *Application of a long-range terrestrial laser scanner to a detailed rockfall study at Vall de Núria (eastern Pyrenees, Spain)*. Eng. Geol., **88,** 136-148, doi: 10.1016/j.enggeo.2006.09.012.

Agliardi F., Crosta G. and Zanchi A.; 2001: *Structural constraints on deep-seated slope deformation kinematics*. Eng. Geol., **59,** 83-102, doi: 10.1016/S0013-7952(00)00066-1.

Angeli M.G., Pasuto A. and Silvano S.; 2000: *A critical review of landslide monitoring experiences*. Eng. Geol., **55,** 133-147, doi: 10.1016/S0013-7952(99)00122-2.

Bremer M. and Sass O.; 2012: *Combining air borne and terrestrial laser scanning for quantifying erosion and deposition by a debris flow event*. Geomorphol., **138,** 49-60, doi: 10.1016/j.geomorph.2011.08.024.

Casson B., Delacourt C. and Allemand P.; 2005: *Contribution of multi-temporal sensing images to characterize landslide slip surface-application to the La Clapière landslide (France)*. Nat. Hazards Earth Syst. Sci., **5,** 425-437, doi: 10.5194/nhess-5-425-2005.

Crosta G.B. and Agliardi F.; 2002: *How to obtain alert velocity thresholds for large rockslides*. Phys. Chem. Earth A/B/C, **27,** 1557-1565, doi: 10.1016/S1474-7065(02)00177-8.

Delacourt C., Allemand P., Berthier E., Raucoules D., Casson B., Grandjean P., Pambrun C. and Varel E.; 2007: *Remote-sensing techniques for analysing landslide kinematics: a review*. Bull. Soc. Geol., **178**, 89-100, doi: 10.2113/gssgfbull.178.2.89.

Deliormanli A.H., Maerz N.H. and Otoo J.; 2014: *Using terrestrial 3D laser scanning and optical methods to determine orientations of discontinuities at a granite quarry*. Int. J. Rock Mech. Min. Sci., **66,** 41-48, doi: 10.1016/j.ijrmms.2013.12.007.

Du J. and Teng H.; 2007: *3D laser scanning and GPS technology for landslide earthwork volume estimation*. Autom. Constr., **16,** 657-663, doi: 10.1016/j.autcon.2006.11.002.

Dunning S.A., Massey C.I. and Rosser N.J.; 2009: *Structural and geomorphological features of landslides in the Bhutan Himalaya derived from terrestrial laser scanning*. Geomorphol., **103,** 17-29, doi: 10.1016/j.geomorph.2008.04.013.

Eberhardt E., Watson A. and Loew S.; 2010: *Improving the interpretation of slope monitoring and early warning data through better understanding of complex deep-seated landslide failure mechanisms*. In: Proc., 10th Int. Symp. on Landslides and Engineered Slopes, Xi'an, China, pp. 39-51, doi: 10.1201/9780203885284-c3.

Fukuzono T.; 1990: *Recent studies on time prediction of slope failure*. Landslide News, **4**, 9-12.

Goodman R.E.; 1980: *Introduction to rock mechanics, chapter 8*. Wiley, Toronto, Canada, pp. 254-287.

Goodman R.E.; 1989: *Introduction to rock mechanics (2nd edition)*. Wiley, New York, NY, USA, 562 pp.

Goodman R.E. and Bray J.W.; 1976: *Toppling of rock slopes*. In: Proc., Specialty Conference on Rock Engineering for Foundations and Slopes, Boulder, CO, USA, vol. 2, pp. 201-234.

Hoek E. and Bray J.W.; 1981: *Rock slope engineering (3rd ed)*. The Institution of Mining and Metallurgy, London, UK, 358 pp.

Hu H., Fernandez-Steeger T.M., Dong M. and Azzam R.; 2012: *Numerical modeling of LiDAR-based geological model for landslide analysis*. Autom. Constr., **24,** 184-193, doi: 10.1016/j.autcon.2012.03.001.

Hudson J.A. and Harrison J.P.; 1997: E*ngineering rock mechanics: an introduction to principles (1st ed)*. Elsevier Sci., Oxford, UK, 456 pp.

Inci U.; 1998: *Lignite and carbonate deposition in Middle Lignite succession of the Soma Formation, Soma coalfield, western Turkey*. Int. J. Coal Geol., **37**, 287-313, doi: 10.1016/S0166-5162(98)00010-X.

Inci U.; 2002: *Depositional evolution of Miocene coal successions in the Soma coalfield, western Turkey*. Int. J. Coal Geol., **51**, 1-29, doi: 10.1016/S0166-5162(01)00066-0.

Jaselskis E.J., Gao Z. and Walters R.C.; 2005: *Improving transportation projects using laser scanning*. J. Constr. Eng. Manage., **131**, 377-384, doi: 10.1061/(ASCE)0733-364(2005)131:3(377)#sthash.YUbcPb2v.dpuf.

Kaiser P.; 1993: *Deformation monitoring for stability assessment of underground openings*. Compress. Rock Eng., **4,** 607-630, doi: 10.1016/B978-0-08-042067-7.50028-3.

Kromer R.A., Hutchinson D.J., Lato M.J., Gauthier D. and Edwards T.; 2015: *Identifying rock slope failure precursors using LiDAR for transportation corridor hazard management*. Eng. Geol., **195,** 93-103, doi: 10.1016/j.enggeo.2015.05.012.

Lato M., Diederichs M.S., Hutchinson D.J. and Harrap R.; 2009: *Optimization of LiDAR scanning and processing for automated structural evaluation of discontinuities in rock masses*. Int. J. Rock Mech. Min. Sci., **46,** 194-199, doi: 10.1016/j.ijrmms.2008.04.007.

Matheson G.D.; 1989: *The collection and use of field discontinuity data in rock slope design*. Q. J. Eng. Geol., **22,** 19-30.

Nebert K.; 1978: *Linyit içeren Soma Neojen bölgesi, Batı Anadolu*. MTA Derg., **90**, 20-69, (in Turkish).

Nishii R. and Matsuoka N.; 2010: *Monitoring rapid head scarp movement in an alpine rockslide*. Eng. Geol., **115,** 49-57, doi: 10.1016/j.enggeo.2010.06.014.

Oppikofer T., Jaboyedoff M. and Kreusen H-R.; 2008: *Collapse at the eastern Eiger flank in the Swiss Alps*. Nat. Geosci., **8,** 531-535, doi: 10.1038/ngeo258.

Ozdogan M.V. and Deliormanli A.H.; 2016: *Monitoring of landslide at Tuncbilek open pit stripping area with terrestrial laser scanner and optical images*. IOP Conf. Series: Earth and Environ. Sci., **44**, 1-6, doi: 10.1088/1755-1315/44/4/042035.

Petley D.N.; 2004: *The evolution of slope failures: mechanisms of rupture propagation*. Nat. Hazards Earth Syst. Sci., **4,** 147-152, doi: 10.5194/nhess-4-147-2004.

Petley D.N., Bulmer M.H. and Murphy W.; 2002: P*atterns of movement in rotational and translational landslides*. Geol., **30**, 719-722, doi: 10.1130/0091-7613(2002)030<0719:POMIRA>2.0.CO;2.

Pettifer G.S. and Fookes P.G.; 1994: *A revision of the graphical method for assessing the excavatability of rock*. Q. J. Eng. Geol., **27,** 145-164.

Priest S.D.; 1980: *The use of inclined hemisphere projection methods for the determination of kinematic feasibility slide direction and volume of rock blocks*. Int. J. Rock Mech. Min. Sci. Geomech. Abstr., **17,** 1-23.

Richards L.R., Leg G.M.M. and Whittle R.A.; 1978: *Appraisal of stability conditions in rock slopes*. In: Bell F.G. (ed), Foundation Engineering in Difficult Ground, Newness-Butterworths London, UK, pp. 449-512.

Rocscience Inc; 2014: *Dips*. < www.rocscience.com/rocscience/products/dips >, Toronto, Canada.

Rose N.D. and Hungr O.; 2007: *Forecasting potential rock slope failure in open pit mines using the inverse-velocity method*. Int. J. Rock Mech. Min. Sci., **44,** 308-320, doi: 10.1016/j.ijrmms.2006.07.014.

Rosser N., Lim M., Petley D., Dunning S. and Allison R.; 2007: *Patterns of precursory rockfall prior to slope failure*. J. Geophys. Res., **112,** F04014, doi: 10.1029/2006JF000642.

Royán M.J., Abellán A., Jaboyedoff M., Vilaplana J.M. and Calvet J.; 2013: *Spatio-temporal analysis of rock fall pre-failure deformation using Terrestrial LiDAR*. Landslides, **11,** 697-709, doi: 10.1007/s10346-013-0442-0.

Stead D. and Wolter A.; 2015: *A critical review of rock slope failure mechanisms: the importance of structural geology*. J. Struct. Geol., **74,** 1-23.

Stead D., Eberhardt E. and Coggan J.S.; 2006: *Developments in the characterization of complex rock slope deformation and failure using numerical modelling techniques*. Eng. Geol., **83,** 217-235, doi: 10.1016/j.enggeo.2005.06.033.

Szwedzicki T.; 2003: *Rock mass behaviour prior to failure*. Int. J. Rock Mech. Min. Sci., **40**, 573-584, doi: 10.1016/S1365-1609(03)00023-6.

Tercan A.E., Unver B., Hindistan M.A., Ertunc G., Atalay F., Unal S. and Kıllıoğlu Y.; 2013: *Seam modeling and resource estimation in the coalfields of western Anatolia*. Int. J. Coal Geol., **112,** 94-106, doi: 10.1016/j.coal.2012.10.006.

Teza G., Pesci A., Genevois R. and Galgaro A.; 2008: *Characterization of landslide ground surface kinematics from terrestrial laser scanning and strain field computation*. Geomorphol., **97,** 424-437, doi: 10.1016/j.geomorph.2007.09.003.

Travelletti J., Malet J.P. and Delacourt C.; 2014: *Image-basedcorrelation of laser scanning point cloud time series for landslide monitoring*. Int. J. Appl. Earth Obs. Geoinf., **32,** 1-18, doi: 10.1016/j.jag.2014.03.022.

Wyllie D.C. and Mah C.W.; 2004: *Rock slope engineering: civil and mining, 4th ed*. Spon Press, New York, NY, USA, 455 pp.

Zheng D., Frost J.D., Huang R.Q. and Liu F.Z.; 2015: *Failure process and modes of rock fall induced by underground mining: a case study of Kaiyang Phosphorite Mine rockfalls*. Eng. Geol., **197**, 145-157, doi: 10.1016/j.enggeo.2015.08.011.

Corresponding author: Ahmet Hamdi Deliormanli
Department of Mining Engineering, Dokuz Eylul University
Adatepe, Dogus street 207-I, 35390 Buca-Izmir, Turkey
Phone: +90 505 610 7439; e-mail: ahmet.deliormanli@deu.edu.tr